Volumetric Obscurance as a New Tool to Better Visualize Relief from Digital Elevation Models

Tanguy Rolland, Fabrice Monna, Jean-François Buoncristiani, Jérôme Magail, Yury Esin, Benjamin Bohard, Carmela Chateau-Smith

▶ **To cite this version:**

Tanguy Rolland, Fabrice Monna, Jean-François Buoncristiani, Jérôme Magail, Yury Esin, et al.. Volumetric Obscurance as a New Tool to Better Visualize Relief from Digital Elevation Models. Remote Sensing, 2022, 14 (4), pp.941. 10.3390/rs14040941 . hal-03576510

HAL Id: hal-03576510
https://hal.science/hal-03576510v1

Submitted on 16 Feb 2022

HAL is a multi-disciplinary open access archive for the deposit and dissemination of scientific research documents, whether they are published or not. The documents may come from teaching and research institutions in France or abroad, or from public or private research centers.

L'archive ouverte pluridisciplinaire **HAL**, est destinée au dépôt et à la diffusion de documents scientifiques de niveau recherche, publiés ou non, émanant des établissements d'enseignement et de recherche français ou étrangers, des laboratoires publics ou privés.

remote sensing

MDPI

Article

Volumetric Obscurance as a New Tool to Better Visualize Relief from Digital Elevation Models

Tanguy Rolland [1,*], Fabrice Monna [1], Jean François Buoncristiani [2], Jérôme Magail [3], Yury Esin [4], Benjamin Bohard [5] and Carmela Chateau-Smith [6]

[1] ARTEHIS, UMR CNRS 6298, Université de Bourgogne–Franche Comté, 6 Boulevard Gabriel, Bat. Gabriel, 21000 Dijon, France; fabrice.monna@u-bourgogne.fr
[2] Biogéosciences UMR CNRS 6282, Université de Bourgogne–Franche Comté, 6 Boulevard Gabriel, Bat. Ga-briel, 21000 Dijon, France; jfbuon@u-bourgogne.fr
[3] Musée d'Anthropologie préhistorique de Monaco, 56 bis, boulevard du Jardin exotique, 98000 MC, Monaco; jerome.magail@map-mc.com
[4] Khakassian Research Institute for Language, Literature and History, 23, Shchetinkin Street, Abakan 655017, Republic of Khakassia, Russia; esin2006@yandex.ru
[5] Cadoles, 29 bis rue de l'Arquebuse, 21000 Dijon, France; bbohard@cadoles.com
[6] CPTC, EA4178, Université de Bourgogne–Franche Comté, 4, boulevard Gabriel, 21000 Dijon, France; carmela.chateau@u-bourgogne.fr
* Correspondence: tanguy.rolland@u-bourgogne.fr; Tel.: +33-(0)-380395797

Abstract: The use of digital elevation models (DEMs) has become much more widespread in recent years, thanks to technological developments that facilitate their creation and availability. To exploit these data, a set of processing techniques has been developed to reveal the characteristic structures of the relief. This paper presents a new method based on the volumetric approach, and two derivatives. These methods are evaluated on three DEMs at different resolutions and scales: a freely accessible DEM from JAXA DEM covering part of North-East Tanzania, a DEM corresponding to rock art in Siberia, and a DEM of an archaeological Bronze Age funeral structure. Our results show that with the volumetric approach, concave and convex areas are clearly visible, with contrast marking slope breaks, while the overall relief is attenuated. Furthermore, the use of volume reduces the impact of noise, which can occur when processing is based on sky visibility (e.g., sky-view factor or positive openness) or second derivatives. Finally, the volumetric approach allows the implementation of a vertical exaggeration factor, the result of which will enhance the particular characteristics of the landscape. The present study comes with a standalone executable program for Windows, a QGIS plugin, and the scripts written in Python, including GPU compute capability (via CUDA) for faster processing.

Keywords: digital elevation model (DEM); relief mapping; visualization; volumetric approach; data processing

Citation: Rolland, T.; Monna, F.; Buoncristiani, J.F.; Magail, J.; Esin, Y.; Bohard, B.; Chateau-Smith, C. Volumetric Obscurance as a New Tool to Better Visualize Relief from Digital Elevation Models. *Remote Sens.* **2022**, *14*, 941. https://doi.org/10.3390/rs14040941

Academic Editor: Peter Reinartz

Received: 07 December 2021
Accepted: 09 February 2022
Published: 15 February 2022

Publisher's Note: MDPI stays neutral with regard to jurisdictional claims in published maps and institutional affiliations.

Copyright: © 2022 by the author. Licensee MDPI, Basel, Switzerland. This article is an open access article distributed under the terms and conditions of the Creative Commons Attribution (CC BY) license (https://creativecommons.org/licenses/by/4.0/).

1. Introduction

The study of landforms is an essential step in many research fields, such as geomorphology, geology, hydrology, archaeology, civil engineering, and mining. Quantitative analyses are mainly based on digital elevation models (DEMs), a generic term for models including vegetation or human structures (i.e., digital surface model), as well as those describing only ground elevation (i.e., digital terrain model). Both are available in the form of a raster grid. Nowadays, such resources can be produced by many different techniques, with photogrammetry, synthetic aperture radar interferometry (InSAR or IfSAR), and light detection and ranging (LiDAR) among the most common. As recent technological developments have greatly facilitated both acquisition and processing, the production and analysis of DEMs has become a standard, especially since low resolution DEMs covering the entire Earth are freely available from several governmental agencies (e.g., SRTM,

Aster GDEM, and ALOS WORLD 3D 30). A set of procedures has been developed to highlight geomorphological features (e.g., valleys, peaks, and ridges), and elevation anomalies of anthropogenic origin (e.g., ancient or recent quarries, mines, and walls) [1]. These procedures are based on color cast [2], differential geometry including slope and different expressions of curvature [1,3–5], trend removal [6,7], sky visibility [8–10], artificial illumination [11–14], pattern analysis [15], and aspect changes [16], to cite the main algorithms. Each of these tools produces a different picture of the relief, with associated advantages and drawbacks. Note that combining these procedures for a single image may be particularly informative [17].

The widely used analytical hill-shading simulates directional illumination. Its outputs are straightforwardly interpretable and quite effective for revealing small elevation variations on flat surfaces, but they may be inefficient in the case of linear anomalies, parallel to the illumination direction [13]. Topographic Position Index (TPI) is defined as the difference in altitude between a central pixel and the mean of the surrounding cells in the DEM within a radius r [18]. For convenience, the final TPI values are generally standardized (mean equals 0 and standard deviation equals 1). The TPI emphasizes valleys, peaks, and edges well, but fails to provide an overall view of the landscape. Mean curvature is based on second derivatives. It is defined as the average of the two principal (minimal and maximal) curvatures [19]. It varies between positive values for convex and negative for concave landforms, while a zero value denotes a planar surface, steep or horizontal. In that sense, it resembles TPI. Methods like sky-view factor (SVF, [8]) and positive openness (PO, [9,10]) rely on the portion of sky visible from all points. The SVF is based on a hemispherical influence zone, and elevation angles are calculated from the horizon, whereas PO uses a sphere and calculates angles from the nadir. Both are efficient for concave areas [10], but behave differently on convex structures and slopes. They also suffer from sampling, as the portion of visible sky is estimated from a predefined number of directions (usually 8), while the presence of noise, even at a low level, in the close vicinity of the point of interest may produce spurious results. More recently, Hu et al. (2021) focused on changes in aspect direction (downslope direction). The underlying idea is to compute projected aspect change vectors (PACV), quantifying terrain plan concavity and convexity without any need of curvature, which is known to be scale dependent and sensitive to DEM errors. Shadows play an important role in our perception of the world [20,21], which is why analytical hill-shading is so popular. Another method, also based on shading, is ambient occlusion, which has become widely democratized during the past two decades for processing 3D scenes. It was developed in the video-game industry [22–26] to obtain a realistic rendering by darkening the concave parts that naturally receive less light. In its simplest form, ambient occlusion is obtained by simulating ambient light, coming from all directions at the same time. This method soon resulted in a multitude of algorithms for rapid processing of 3D models, all seeking to achieve a good balance between computational needs and quality. One of these algorithms, volumetric obscurance (VO), is based on volumes [23]. It produces a sphere centered on the point of interest, and considers the volume of this sphere outside the 3D mesh as a proxy for illumination.

The aim of this study is to adapt the VO approach, initially designed for 3D models, to the study of DEMs, and to evaluate the resulting outputs by comparing them to those obtained with more classical methods, such as SVF, PO, mean curvature, TPI, and PACV. The effects of two parameters are examined: (*i*) the radius of the sphere determining the influence zone around each cell of the grid, which is an intrinsic parameter of VO, and (*ii*) vertical exaggeration, which is a multiplying factor applied to the DEM values. Three DEMs, with different resolutions, used for different purposes, illustrate the capabilities of the proposed method. The first is used for geomorphological analysis in a volcanic setting in Tanzania. The other two DEMs were produced and processed for archaeological purposes. One represents a carving at a Siberian rock art site, and the other represents funeral structures in the Arkhangai region, Mongolia.

2. Material and Methods

2.1. Corpus

The first DEM used in this study (Figure 1a) was freely obtained from JAXA DEM (provided by AW3D30, JAXA). This DEM, with a 30 m/px resolution, covers a region in the northeast of Tanzania, on the margin of the East African Rift System. It extends from the Serengeti Plain in the west to the Ngorongoro highland in the east, encompassing the Salei Plain. Geomorphologically, this region is very contrasted, with a marked dendritic river pattern, plateaus, and volcanic edifices with steep slopes [27–29].

The other two DEMs used here were produced by photogrammetry with Agisoft Metashape (https://www.agisoft.com/, accessed on October 2020) specifically for archaeological purposes. The Siberian DEM (Figure 1b) illustrates a petroglyph from the Shalabolino rock art site, Minusinsk Basin, which has been well documented in many methodological and stylistic studies [30–34]. This remarkable site exhibits carved and painted figures dating from the Stone Age to the Early Middle Ages [30,31]. The example processed here is a rider from the Tagar culture, dating from the Early Iron Age. It was produced from photographs captured by a Sony DSC-RX100M3. The surface measures 22 × 22 cm², with a resolution of 0.1 mm/px. The depth of the carved parts is approximately 1 mm. The third DEM (Figure 1c) shows one of the larger Mongolian Bronze Age funeral monuments: the khirigsuur Urt Bulag 2, located in the Khanuy River Valley (Figure 1c). This monument is composed of a central stone tumulus (ca. 3 m high), surrounded by hundreds of stone mounds and stone circles. Photographs were captured using a DJI Phantom 3 PRO unmanned aerial vehicle. The entire DEM measures 359 × 426 m², with a resolution of 3 cm/px, and a subset was extracted for further processing (red rectangle in Figure 1c).

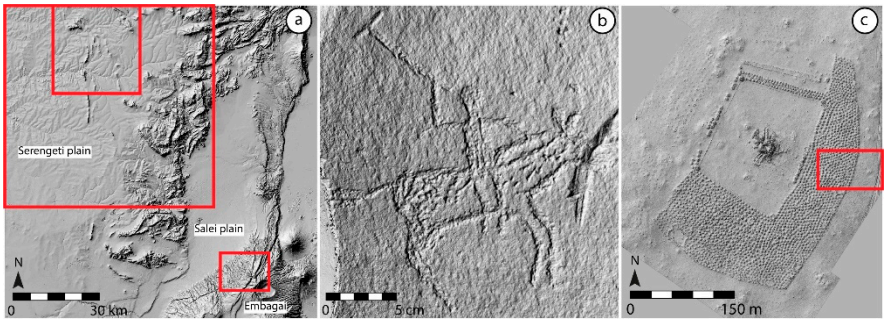

Figure 1. The three DEMs, all processed with analytical hill-shading. Red rectangles indicate specific zones studied. (**a**) DEM of study area in Tanzania. (**b**) DEM of rock art representing a rider, Shalabolino, Siberia. (**c**) DEM of funeral structure, Urt Bulag 2, Mongolia.

2.2. Volumetric Approach

Volumetric Obscurance (VO), which determines the amount of occlusion around a point of interest, *P*, was originally developed for processing 3D models. It was defined as:

$$V(P) = \int_S \rho(d(P,s))O(s)ds \quad (1)$$

Where *S* is a surrounding sample sphere, $O(s)$ an occupancy function that takes the value 0 when *s* is inside the geometry, and is otherwise 1; ρ is a fall-off function, which is defined to be 1 at *P*, possibly d0ecreasing progressively to 0, at a certain distance from *P*, $d(P,s)$. Loos et al. 2010 [23] performed several experiments, and observed that using a complex fall-off function, for instance under a quadratic form, was unnecessary because of the computation cost. These authors, therefore, retained a constant function only. In our case, Volumetric Obscurance is computed after creating a spherical volume around a point of interest (*P*, Figure 2a), from a DEM, and not from a 3D model. The portion of this sphere's volume located above the surface described by the DEM is then calculated (Figure 2b). Two additional processes were developed, based on the hemispherical volume used in

SVF. The process based on the zenith-oriented hemisphere (Figure 2c) will calculate the volume above the surface (VOP: Volumetric Obscurance, "positive"). The process based on the nadir-oriented hemisphere (Figure 2d) will calculate the volume below the surface (VON: Volumetric Obscurance, "negative").

The main difference with VO calculation, as described above in Equation (1), is that volume portions assessed here are normalized to total sphere or hemisphere volumes. The results are, therefore, comprised between 0 and 1, thus facilitating further readings and comparisons.

$$\mathrm{VO} = \frac{\text{sphere volume above surface}}{\text{total sphere volume}}, \mathrm{VO} \in [0,1] \quad (2)$$

$$\mathrm{OP} = \frac{\text{hemisphere volume above surface}}{\text{total hemisphere volume}}, \mathrm{VOP} \in [0,1] \quad (3)$$

$$\mathrm{VON} = \frac{\text{hemisphere volume below surface}}{\text{total hemisphere volume}}, \mathrm{VON} \in [0,1] \quad (4)$$

A line-based strategy is used to approximate these volumes [23]. Segments run perpendicular to the horizon from the landform surface to their intersections with the sphere (Figure 2). Segment lengths are summed for the targeted part: ΣL_{VOi} for VO (Figure 2b), ΣL_{VOPi} for VOP (Figure 2c), and ΣL_{VONi} for VON (Figure 2d). These approximated volumes are normalized using that of the entire sphere (using ΣL_i) for VO, and that of a hemisphere (using ½ ΣL_i) for VOP and VON. Note that VO is linked to VOP and VON by:

$$VO = \frac{VOP - VON}{2} + 0.5 \quad (5)$$

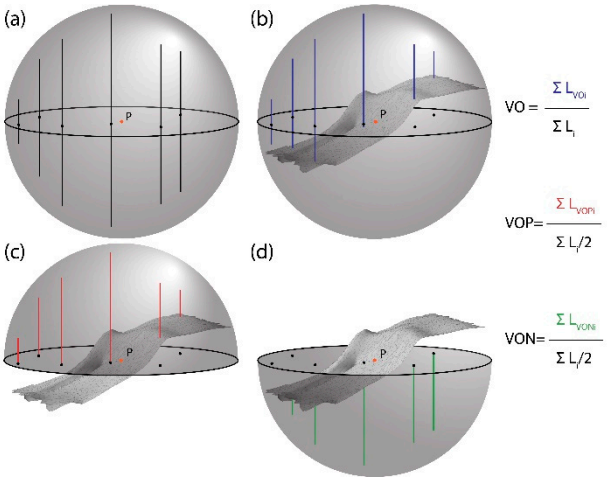

Figure 2. Illustration of the line sampling scheme for the three volumetric approaches, and related equations. Different colored segments are used for each approach: (**a**) black segments sample the sphere volume; (**b**) blue is used for VO calculation; (**c**) red for VOP; (**d**) green for VON.

2.3. Algorithm

The raster format of DEMs is well adapted to line-based volume approximation as each pixel can be used as the starting point to compute a segment length. The first step is to define a grid where each pixel within a circle of radius *r* (Figure 3a) contains the value of the zenith altitude of the hemisphere, h, taking into account the DEM resolution. This grid becomes the reference for segment length calculation in the following (Figure 3b). Consider now the case of any point, P, in a DEM for VO calculation: the second step is to shift the DEM, such that the altitude at P becomes 0 (Figure 3c). The altitude of each pixel of the DEM around P is then subtracted from the altitude of the corresponding pixel in the reference grid (Grid_value) to obtain the altitude of the sphere located above the relief.

If that difference, Δh, is negative (case 1 in Figure 3c), the relief is above the sphere, and the new pixel value is therefore set to 0. When the difference is positive, but less than twice that of the Grid_value (case 2 in Figure 3c), then the new pixel value becomes Δh. Finally, if Δh exceeds twice the value of the grid, the relief is below the sphere (case 3 in Figure 3c), and the new pixel value is set at twice that of the Grid_value. These new values correspond to the L_{VOi} used to compute the value of VO for the point P. This process is repeated for each DEM pixel. Both VOP and VON are computed following the same principles. The only difference between VO and VOP is that Δh is compared to Grid_value, instead of 2 × Grid_value. For VON, the subtraction is reversed, thus calculating segment lengths from below the landform.

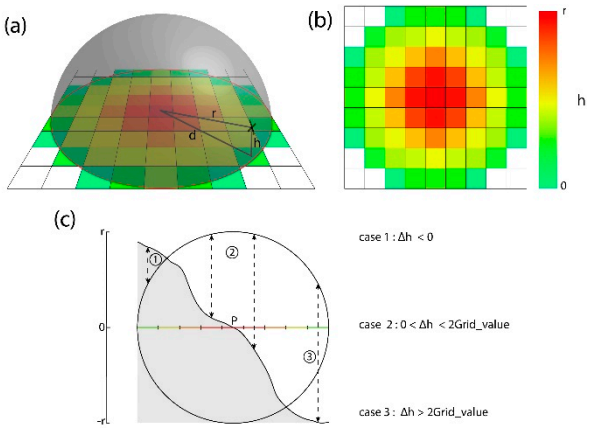

Figure 3. Computational volumetric approaches. (**a**) Representation of hemisphere projection on grid; (**b**) Reference grid with colored values; (**c**) Illustration of the three possible positions of the ground surface in relation to the sphere. Case 1: above the sphere. Case 2: within the sphere. Case 3: below the sphere.

2.4. Implementation

The three methods presented above were implemented in Python, provided here as an open-source script (SM1), as a standalone executable program for Windows (SM2), and as a QGIS 3.X plugin (SM2). The vSky program uses the following Python libraries: PyQT 5.9.2, Numpy 1.16.4, Pillow 6.1.0, Scipy 1.2.1, Cupy 6.0.0, and Gdal 3.0.2. This code allows any projected DEM to be loaded and processed, provided that the resolution is the same in X and Y. Three parameters are tunable: the radius of the sphere and/or hemisphere influence, the strength of smoothing (which is obtained by applying a Gaussian kernel and fast Fourier transform convolution), and the vertical exaggeration (Figure 4). Smoothing and vertical exaggeration optionally pre-process the DEM. The first reduces aliasing and noise by attenuating high-frequency relief, while vertical exaggeration applies a multiplying factor to the altitude, exaggerating or attenuating variations in relief. Vertical exaggeration is often used in combination with analytical hill-shading to adjust the visual aspect. After calculation, results are saved as georeferenced raw data rasters, optionally together with an 8-bit version for each of the three treatments, and an RGB three-channel image combining VO, VOP, and VON. The 8-bit images are produced after linear and saturation stretching within a 2nd–98th percentile interval. In this process, the outputs ϵ [0,1] are remapped to fit the 0–255 range for grayscale rendering. These simplified additional outputs are produced for rapid visual inspection; any further calculation from this documentation should therefore be avoided.

Figure 4. Capture of vSky software, showing a grayscale image of the DEM and its characteristics, as well as the parameters that need to be defined in this method.

3. Experiments

3.1. Algorithm Comparison

In the following, the three new processes—VO, VOP, and VON—are applied to the Tanzanian JAXA DEM and are compared to results from TPI, mean curvature, PO, and SVF (Figure 5a), computed with SAGA GIS (http://www.saga-gis.org/en/index.html, accessed on October 2020). In addition, the correlation matrix between raw outputs is provided in Figure 5b. This specific area was selected because it is among the examples used to introduce the SVF algorithm [8]. To facilitate further comparison, processing was systematically performed without pre-smoothing or vertical exaggeration, and a 300 m influence radius (i.e., 10 pixels) was applied because this value has already been found to be appropriate to study geomorphological features [8]. In the VO output (Figure 5a), the overall perception of the landscape is somewhat lost, as the zones with constant slope values, whether flat or regularly sloping, appear mid-gray (VO ≈ 0.5). Only convex and concave areas are highlighted, where edges, ridges, and protruding parts (VO value > 0.5) tend toward white, and thalwegs and bottoms (VO value < 0.5) tend toward black. The TPI and, to a lesser extent, mean curvature rasters are almost the same as VO ($r_{TPI\text{-}VO}$ = 0.997 and $r_{M.CURV\text{-}VO}$ = 0.924; Figure 5b), at least in the present configuration (i.e., without vertical exaggeration); this point will be discussed later. With VOP, summits and flat areas are essentially white (VOP ≈ 1), while concave parts are darkened (when concavity increases, VOP decreases). Non-null slopes are displayed in mid-gray (Figure 5a). Almost the same results are observed with SVF ($r_{VOP\text{-}SVF}$ = 0.891, Figure 5b), and to some extent with PO ($r_{VOP\text{-}PO}$ = 0.822, Figure 5b), where constant slopes and flat surfaces are represented in similar ways [10]. Although whitish overall, the VON raster exhibits darkened convex

parts (VON decreases when convexity increases) and whitened concave and flat parts (VON ≈ 1), i.e., inversely to the other methods. One could, therefore, suppose that VON in some way produces mirror images of VOP, SVF, and PO. In fact, the situation is more complex; different types of information are extracted. Both SVF and VOP specifically focus on the relief present in the hemisphere above the surface (limited by the horizontal plane passing through the point of interest), while VON is based only on the surface inside the lower hemisphere. The SVF and VOP methods saturate if the relief is flat, and therefore cannot capture convexity (Figure 6). By contrast, although VON is more efficient to describe convex relief, it does not capture concavity, and saturates with flat relief (Figure 6). As a result, poor inverse correlations are observed between VON and SVF ($r_{VON\text{-}SVF}$ = −0.080, Figure 5b) and between VON and VOP ($r_{VON\text{-}VOP}$ = −0.096, Figure 5b). The PO and VO methods take into account everything that is above the relief (Figure 6), including parts below the point of interest. Therefore, they share common elements with VON, which explains why the strength of the linear relationship is greater with PO ($r_{VON\text{-}PO}$ = −0.370), and especially with VO ($r_{VON\text{-}VO}$ = −0.715) (Figure 5b). This is also true for the relationship between VOP and VO, which are positively correlated ($r_{VOP\text{-}VO}$ = 0.765), but convexity cannot be differentiated from flatness by VOP, while VO can describe the full range of relief, from extreme concavity to extreme convexity (Figure 6).

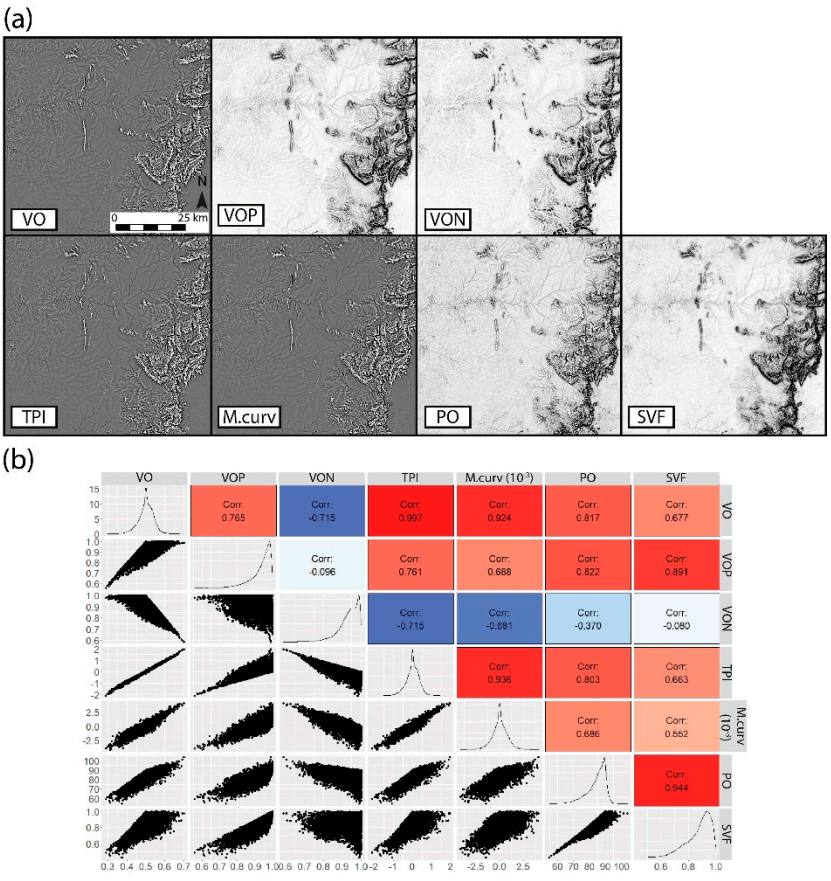

Figure 5. (**a**) Comparison between VO, VOP, VON, TPI, mean curvature (M.curv) PO, and SVF processing applied to the Tanzanian DEM. (**b**) Diagram summarizing pairwise linear correlations for all methods tested. The upper triangle reports the correlation coefficients. The diagonal cells present the distribution values for each method. The lower triangle depicts pairwise scatterplots.

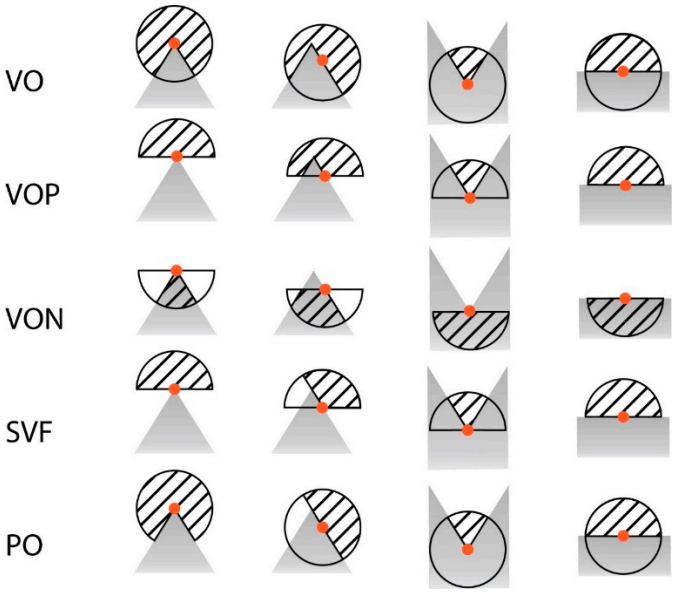

Figure 6. Sketches where hatching depicts the zones taken into account by the VO, VOP, VON, SVF, and PO methods, applied to different topographic cases.

Figure 7 displays a 2.8 km topographic cross-section (AB in Figure 7), oriented SW/NE, across the northern hillside of the Embagai crater, and the values resulting from each method (again with an influence radius of 300 m). The overall shape along the cross section is largely lost (large-scale variations), whatever the processing applied. By contrast, all topographical variations compatible with the set radius are emphasized (smaller-scale variations). This is especially true for VO and VOP, which depict well the subtle altitudinal variations inside the valleys (mark 1 in Figure 7), while the VON algorithm produces the smallest relative amplitude and reacts less than the others to the abrupt changes in altitude (the edge marked 2 in Figure 7). The SVF and PO profiles are noticeably more jagged than those drawn from volumetric approaches, and from TPI and mean curvature (see ridge at mark 3 in Figure 7). The VO, VOP, VON, TPI, and mean curvature processes also produce slightly less sharp images than SVF and PO in Figure 5a. The reason is that the first four methods take into account the entire relief within the radius *r*, and not only the position of the relief limiting the sky (see changes between the first and second columns in Figure 6, and [8,10]). This characteristic is an asset when the point of interest is surrounded by small surface irregularities. The SVF and PO methods, based on visibility, are so sensitive to this issue that a noise remover is introduced as an option in the Relief Visualization Toolbox (RVT) software in order to reduce the deleterious influence of any protruding neighbors blocking the view [8,35].

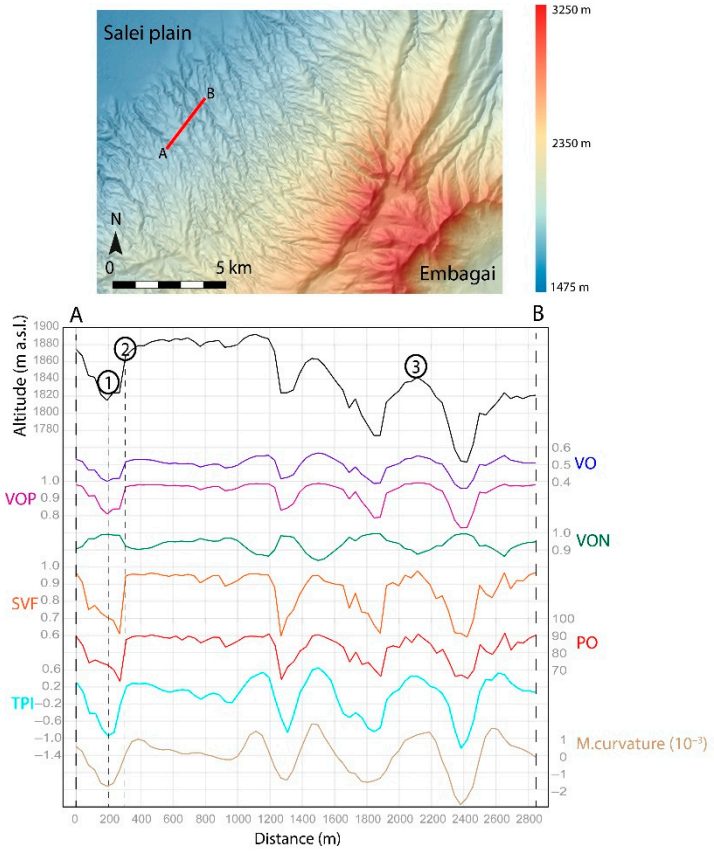

Figure 7. Plot of the topographic section, AB, across the northwestern slope of the Embagai crater, associated with values of VO, VOP, VON, SVF, PO, TPI, and mean curvature (using a 10-pixel radius, except for mean curvature, which uses a 5-pixel radius, as it is better adapted to the study area). The altitude in meters is represented in black, VO in blue, VOP in purple, VON in green, SVF in orange, PO in red, TPI in light blue, and mean curvature in light brown.

3.2. Parameter Influence

3.2.1. Vertical Exaggeration and Sphere Radius

Without vertical exaggeration (a pre-processing step commonly applied to increase relief contrast), results from VO, TPI, and mean curvature appear almost identical (Figure 5). For TPI calculation, if vertical exaggeration is applied by multiplying DEM values by a scalar *a*, the differences in altitude between the point of interest and its surroundings are also multiplied by *a*, (as well as mean and standard deviation) (Figure 8a). Once TPI values are standardized and remapped on to a 0–255 range for a grayscale rendering, the resulting map remains unchanged (Figure 8b). Vertical exaggeration, thus, has no effect on TPI, or on mean curvature, for the same reason. For VO, the situation is quite different: when the topography changes, the influence zone (the sphere) remains the same (Figure 8a). Consequently, the volume of the sphere above the DEM is affected by vertical exaggeration, making this process more versatile than TPI and mean curvature because it can be adapted to a greater variety of situations (Figure 8b).

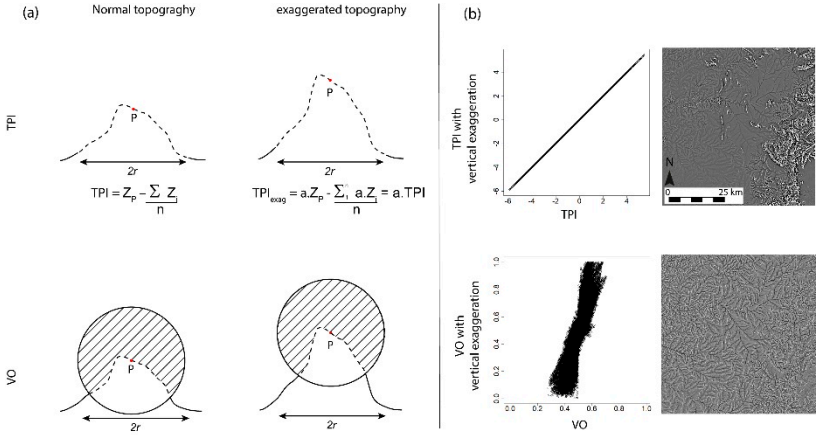

Figure 8. The TPI and VO methods, without exaggeration and with exaggeration, applied on part of the Tanzanian DEM. (**a**) Theoretical topographic profiles, without exaggeration and with x 2 exaggeration, for TPI and VO; (**b**) Scatterplots without exaggeration vs. with exaggeration (a = 1000), and resulting DEM.

Beside optional vertical exaggeration, volumetric methods basically possess one key tunable parameter, the sphere radius, which must be adapted to the size of the features to be highlighted, as with SVF and PO [8,10]. To examine the combined influence of vertical exaggeration and sphere radius, the Shalabolino rock art DEM (resolution 0.1 mm/px) was processed with VO by crossing three values for the r radius: 5, 20, and 40 pixels (equivalent to 0.5, 2 and 4 mm), with three vertical exaggerations: none (i.e. ×1), ×5, and ×20 (Figure 9a–i). The tiniest, sub-horizontal cracks near the rider's feet and the horse's rump are identified at the smallest radius, corresponding to 0.5 mm, but not with the two other radii, which nevertheless better isolate the rider and the steed, at the expense of overall smoothing (Figure 9a, see also SM3 for a zoomable version of Figure 9). Exaggerating the relief allows better delimitation of the bottoms of the engraved parts, but also an increase in the salt-and-pepper effect, due to irregularities in the rock surface (see the upper part of the DEM, in particular in Figure 9e,f,i). The optimal adjustment between radius and vertical exaggeration needs to be sought in relation to the purpose: good perception of the shape engraving, or a more detailed focus on how the carving was made, including the surface condition of the rock.

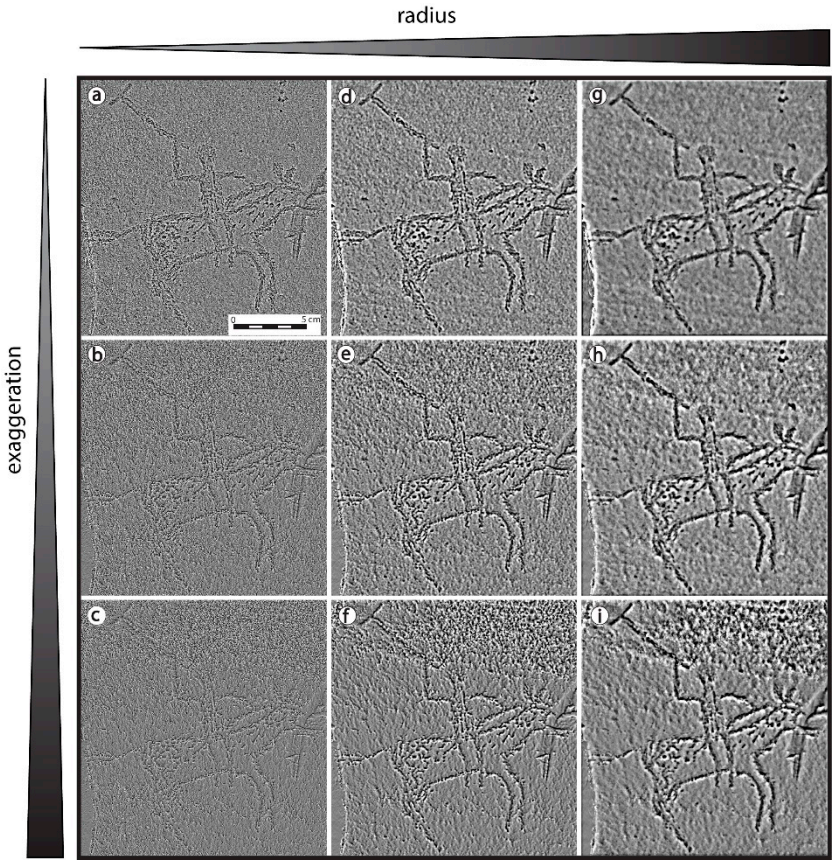

Figure 9. Resulting combinations between influence radius of the sphere and vertical exaggeration for the Shalabolino DEM, processed with VO. Columns correspond to sphere radius values of 5 px (i.e. 0.5 mm), 20 px (2 mm), and 40 px (4 mm). Rows correspond to vertical exaggeration factors of 1 (no exaggeration), 5, and 20.

The hydrologic network of the Serengeti plain provides another example to demonstrate the capabilities of vertical exaggeration applied before VO calculation (Figure 10). Analytical hill-shading was processed without exaggeration to facilitate good understanding of the topography (Figure 10a), while a factor of 1000 was applied before computing VO, SVF, and PO (Figure 10b–d), with a 10-pixel radius, and without pre-smoothing or noise removal. The hydrologic network is revealed whatever the approach, and the valley bottoms are well marked in all cases, as expected. However, the VO image is crisper with narrower talwegs (Figure 10b). The SVF and PO rasters exhibit a more pronounced salt-and-pepper effect, due to the greater sensitivity of these algorithms to noise, as mentioned above (Figure 10c–d). Hu et al. (2021) [16] suggested using changes in aspect (namely PACV) to quantify concavity and convexity from DEMs, thus better identifying ridges and valleys. Here, PACV was computed using a modified version of the Python scripts made available by Hu et al. (2021) at https://github.com/NJNU-DTA/PACV (accessed on October 2020) (Figure 10e). Interestingly, an equivalent output can be obtained with the VO algorithm, when the DEM is adequately smoothed and exaggerated (Figure 10f). As PACV is not scale dependent, exaggeration has no effect on its output, whereas VO can be freely tuned using exaggeration for more versatility.

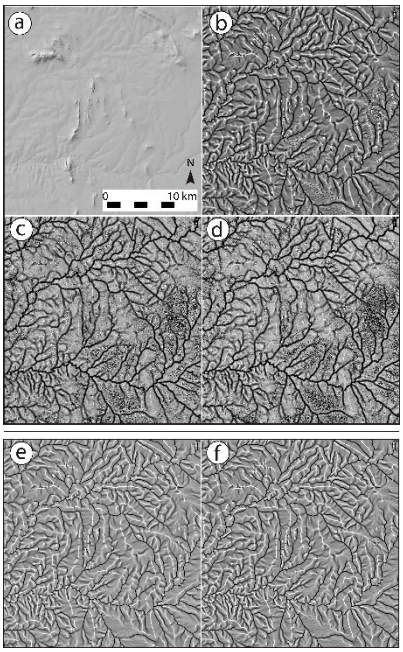

Figure 10. Tanzanian DEM subset on the Serengeti Plain, processed by (**a**) analytical hill-shading without vertical exaggeration, (**b**) VO, (**c**) SVF, (**d**) PO, with vertical exaggeration of 1000 and a radius of 10 px, corresponding to 300 m; (**e**) PACV from a non-exaggerated DEM, and an aspect raster map with a radius of 5 px, (**f**) VO with vertical exaggeration of 1000, a radius of 5 px, and a smooth factor of 10.

3.2.2. VO as Feature Input for Automatic Recognition

The DEMs are often pre-processed to bring out more clearly the particular signature of the features sought, such as crater ridges [36,37], archaeological structures [38,39], roads [40], and valley embankments related to mining [41]. As previously shown, VO provides well-contrasted results at the level of slope breaks, making it possible to identify ridges, valley bottoms, and positive and negative anomalies, thus providing a potentially effective source for automatic detection. As an example, the stones are clearly identifiable from every volumetric output (i.e., VO, VOP, VON) processed on part of the Urt Bulag 2 DEM (Figure 11a–c). Interestingly, these three processes can be combined to form a single RGB image (Figure 11d), where processing fills each of the color channels. Flat parts appear in light blue, convex parts (mound tops) in yellow, and concave parts in dark blue. Red corresponds to strong slopes (>25–30°). Such an image should not be used for calculation, but it may be more straightforward to interpret, at a glance, without closely examining VO, VOP, and VON, one after the other. Interestingly, it may be used as input for automatic detection of structures, with algorithms using RGB images, such as object detection via deep learning [42].

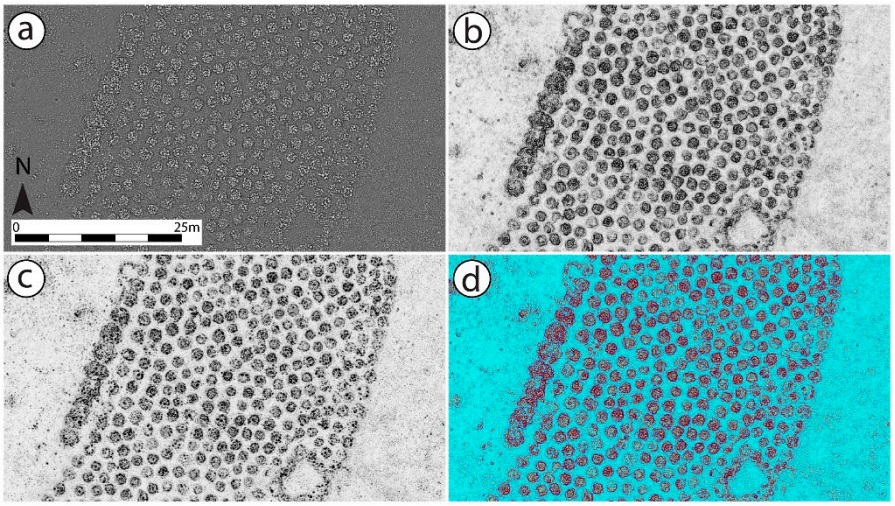

Figure 11. Subset of the Urt Bulag 2 DEM, processed with (**a**) VO, (**b**) VOP, and (**c**) VON; (**d**) represents an RGB combination of the three processes, filling each of the RGB channels. All methods use a radius of 6 px (18 cm), without exaggeration.

4. Conclusion

This study introduces three new DEM processing methods based on volumetric approaches: VO, VOP, and VON. The principle is to consider the entire volume above or below the relief within the area of influence, which is spherical for VO, and hemispherical for VOP and VON. Although the procedures proposed here share common properties with existing algorithms, they possess several interesting assets. First, there is no need to sample a set of directions, as with SVF and PO calculation. Second, the assessment of a volume instead of a sky-limiting relief is much less affected by possible noise, a frequent problem in the case of SVF and PO, which may require nearest neighbors to be ignored. That is also true because the volumetric approach does not require derivatives, which generally suffer from numerical instability. Finally, vertical exaggeration, which has no effect on TPI, mean curvature, and PACV, can be applied before VO computation to enhance specific landscape features. The VO essentially yields gray results, attenuating the overall relief, with strong black-white contrast on slope breaks. Its interpretation may appear less intuitive than that provided by analytical hill-shading, but it is much more specific (and informative) for relief anomalies at a given scale; note that VON and VOP can also be examined in combination, to better apprehend the overall landform. These three new processing tools can be efficiently used in all research fields exploiting DEMs, and at any scale, for semi-automated detection based on thresholding or deep learning. Advantageously, they can provide almost the same information as the traditional processing tools (SVF, PO, TPI, mean curvature, and the more recent PACV approach) by simply using adequate tunings, which are limited to only three parameters: level of smoothing, exaggeration, and radius. A standalone executable Windows program, which includes GPU compute capability (via CUDA) for faster processing, together with a QGIS plugin, the Python snippet, and an accompanying user manual are freely obtainable in (SM1-2). Such availability should promote testing, and hopefully, dissemination to a broader audience for research purposes.

Supplementary Materials: The following supporting information can be downloaded at: : https://gitlab.huma-num.fr/fmonna/vsky/-/tree/Paper_Supp_Mat. SM1: Python open-source script of vSky. SM2: Standalone executable version of vSky for Windows with user guide and DEMs examples as well as the QGIS 3.X plugin of vSky. SM3: Full resolution version of the figure 9.

Author Contributions: Conceptualization, T.R. and F.M.; methodology, T.R., F.M and J.F.B.; software, F.M. and B.B.; validation, T.R., F.M. and J.F.B.; formal analysis, T.R. and F.M.; data curation, B.B.; writing—original draft preparation, T.R., F.M. and J.F.B.; writing—review and editing, T.R.,

F.M. J.F.B., J.M., Y.E., B.B. and C.C.-S.; visualization, T.R.; supervision, T.R. and F.M.; funding acquisition, F.M. and J.M. All authors have read and agreed to the published version of the manuscript.

Funding: This research and APC were funded by the Joint Mission Mongolia–Monaco and the project ROSAS (uB-FC and RNMSH).

Data Availability Statement: ALOS/PRISM AW3D30: https://doi.org/10.5069/G94M92HB.

Acknowledgments: This research was funded by the Joint Mission Mongolia–Monaco and the project ROSAS (uB-FC and RNMSH). The data used for this paper were provided by ALOS/PRISM AW3D30 of the Japan Aerospace Exploration Agency and the joint Mission Mongolia–Monaco. We are grateful for comments by the anonymous reviewers, which have greatly improved the manuscript.

Conflicts of Interest: The authors declare no conflict of interest.

References

1. Wood, J. *The Geomorphological Characterisation of Digital Elevation Models*; University of Leicester: Leicester, UK, 1996.
2. Challis, K. Airborne laser altimetry in alluviated landscapes. *Archaeol. Prospect.* **2006**, *13*, 103–127.
3. Smith, M.; Goodchild, M.F.; Longley, P.A. *Geospatial Analysis: A Comprehensive Guide to Principles, Techniques and Software Tools*; Matador: Leicester, UK, 2009.
4. Longley, P. (Ed.) *Geographic Information Systems & Science*, 3rd ed.; Fully Updated; Wiley: Hoboken, NJ, USA, 2011.
5. Minár, J.; Evans, I.S.; Jenčo, M. A comprehensive system of definitions of land surface (topographic) curvatures, with implications for their application in geoscience modelling and prediction. *Earth-Sci. Rev.* **2020**, *211*, 103414.
6. Hesse, R. LiDAR-derived Local Relief Models—A new tool for archaeological prospection. *Archaeol. Prospect.* **2010**, *17*, 67–72.
7. Reitberger, J.; Krzystek, P.; Stilla, U. Analysis of full waveform LIDAR data for the classification of deciduous and coniferous trees. *Int. J. Remote Sens.* **2008**, *29*, 1407–1431.
8. Zakšek, K.; Oštir, K.; Kokalj, Ž. Sky-View Factor as a Relief Visualization Technique. *Remote Sens.* **2011**, *3*, 398–415.
9. Yokoyama, R.; Shirasawa, M.; Pike, R.J. Visualizing Topography by Openness: A New Application of Image Processing to Digital Elevation Models. *Photogramm. Eng. Remote Sens.* **2002**, *68*, 257–265.
10. Doneus, M. Openness as Visualization Technique for Interpretative Mapping of Airborne Lidar Derived Digital Terrain Models. *Remote Sens.* **2013**, *5*, 6427–6442.
11. Horn, B.K.P. Hill shading and the reflectance map. *Proc IEEE* **1981**, *69*, 14–47.
12. Hobbs, K.F. An investigation of RGB multi-band shading for relief visualisation. *Int. J. Appl. Earth Obs. Geoinf.* **1999**, *1*, 181–186.
13. Devereux, B.J.; Amable, G.S.; Crow, P. Visualisation of LiDAR terrain models for archaeological feature detection. *Antiquity* **2008**, *82*, 470–479.
14. Kennelly, P.J.; Stewart, A.J. General sky models for illuminating terrains. *Int. J. Geogr. Inf. Sci.* **2014**, *28*, 383–406.
15. Jasiewicz, J.; Stepinski, T.F. Geomorphons—A pattern recognition approach to classification and mapping of landforms. *Geomorphology* **2013**, *182*, 147–156.
16. Hu, G.; Dai, W.; Li, S.; Xiong, L.; Tang, G.; Strobl, J. Quantification of terrain plan concavity and convexity using aspect vectors from digital elevation models. *Geomorphology* **2021**, *375*, 107553.
17. Kennelly, P.J. Terrain maps displaying hill-shading with curvature. *Geomorphology* **2008**, *102*, 567–577.
18. Weiss, A.D. *Topographic Position and Landforms Analysis*; The Nature Conservancy: San Diego, CA, USA, 2001.
19. Grosse-Brauckmann, K. Triply periodic minimal and constant mean curvature surfaces. *Interface Focus* **2012**, *2*, 582–588.
20. Langer, M.S.; Zucker, S.W. Shape-from-shading on a cloudy day. *J. Opt. Soc. Am. A* **1994**, *11*, 467.
21. Phong, B.T. Illumination for computer generated pictures. *Commun. ACM* **1975**, *18*, 311–317.
22. Mittring, M. *Finding Next Gen: CryEngine 2. ACM SIGGRAPH 2007 Courses—SIGGRAPH 07 [Internet]*; ACM Press: San Diego, CA, USA, 2007 [cited 2021 Mar 29]. p. 97. Available online: http://dl.acm.org/citation.cfm?doid=1281500.1281671 (October 2020).
23. Loos, B.J.; Sloan, P.-P. *Volumetric Obscurance. Proc ACM SIGGRAPH Symp Interact 3D Graph Games—I3D 10 [Internet]*; ACM Press: Washington, DC, USA, 2010 [cited 2021 Mar 29]. p. 151. Available online: http://dl.acm.org/citation.cfm?doid=1730804.1730829 (October 2020).
24. McGuire, M.; Osman, B.; Bukowski, M.; Hennessy, P. *The Alchemy Screen-Space Ambient Obscurance Algorithm. Proc ACM SIGGRAPH Symp High Perform Graph—HPG 11 [Internet]*; ACM Press: Vancouver, BC, Canada, 2011 [cited 2021 Mar 29]. p. 25. Available online: http://dl.acm.org/citation.cfm?doid=2018323.2018327 (October 2020).
25. Holden, D.; Saito, J.; Komura, T. *Neural Network Ambient Occlusion. SIGGRAPH ASIA 2016 Tech Briefs [Internet]*; ACM: Macau, 2016 [cited 2021 Mar 29]. p. 1–4. Available online: https://dl.acm.org/doi/10.1145/3005358.3005387 (October 2020).
26. Bokšanský, J.; Pospíšil, A.; Bittner, J. VAO++: Practical Volumetric Ambient Occlusion for Games. In *Eurographics Symposium on Rendering: Experimental Ideas & Implementations*; The Eurographics Association, Dublin, Ireland, 2017, 31-39.
27. Hay, R.L. *Geology of the Olduvai Gorge: A Study of Sedimentation in a Semiarid Basin*; University of California Press: Berkeley, CA, USA, 1976.

28. Hay, R.L.; Kyser, T.K. Chemical sedimentology and paleoenvironmental history of Lake Olduvai, a Pliocene lake in northern Tanzania. *GSA Bull.* **2001**, *113*, 1505–1521.
29. Dawson, J.B. *The Gregory Rift Valley and Neogene-Recent-Volcanoes of Northern Tanzania*; Geological Society of London: London, UK, 2008.
30. Pyatkin, B.N.; Martinov, A.I. *Shalabolinskie Petroglify*; Izd-vo Krasnoyarskogo Universiteta: Krasnoyarsk, Russia, 1985.
31. Pyatkin, B.N. The Shalabolino petroglyphs on the river Tuba (middle Yenisei). *Int. Newsl. Rock Art* **1998**, *20*, 26–30.
32. Delvet, E. *Recent Rock art Studies in Northern Eurasia, 2005–2009*; Oxbow: Oxford, UK; David Brown Book Company [Distributor]: Oakville, CT, USA, 2012; pp. 124–48.
33. Zotkina, L.V. On the Methodology of Studying Palimpsests in Rock Art: The Case of the Shalabolino Rock Art Site, Krasnoyarsk Territory. *Archaeol. Ethnol. Anthropol. Eurasia* **2019**, *47*, 93–102.
34. Zotkina, L.V.; Kovalev, V.S. Lithic or metal tools: Techno-traceological and 3D analysis of rock art. *Digit Appl. Archaeol. Cult. Herit.* **2019**, *13*, e00099.
35. Kokalj, Ž.; Somrak, M. Why Not a Single Image? Combining Visualizations to Facilitate Fieldwork and On-Screen Mapping. *Remote Sens.* **2019**, *11*, 747.
36. Gallwey, J.; Eyre, M.; Tonkins, M.; Coggan, J. Bringing Lunar LiDAR Back Down to Earth: Mapping Our Industrial Heritage through Deep Transfer Learning. *Remote Sens.* **2019**, *11*, 1994.
37. Liu, Q.; Cheng, W.; Yan, G.; Zhao, Y.; Liu, J. A Machine Learning Approach to Crater Classification from Topographic Data. *Remote Sens.* **2019**, *11*, 2594.
38. Monna, F.; Magail, J.; Rolland, T.; Navarro, N.; Wilczek, J.; Gantulga, J.-O.; Esin, Y.; Granjon, L.; Allard, A.-C.; Chateau-Smith, C. Machine learning for rapid mapping of archaeological structures made of dry stones—Example of burial monuments from the Khirgisuur culture, Mongolia–. *J. Cult. Herit.* **2020**, *43*, 118–128.
39. Soroush, M.; Mehrtash, A.; Khazraee, E.; Ur, J.A. Deep Learning in Archaeological Remote Sensing: Automated Qanat Detection in the Kurdistan Region of Iraq. *Remote Sens.* **2020**, *12*, 500.
40. Zakariya Jasim, O. Using of machines learning in extraction of urban roads from DEM of LIDAR data: Case study at Baghdad expressways, Iraq. *Period. Eng. Nat. Sci. PEN* **2019**, *7*, 1710.
41. Maxwell, A.E.; Pourmohammadi, P.; Poyner, J.D. Mapping the Topographic Features of Mining-Related Valley Fills Using Mask R-CNN Deep Learning and Digital Elevation Data. *Remote Sens.* **2020**, *12*, 547.
42. Zhao, Z.-Q.; Zheng, P.; Xu, S.; Wu, X. Object Detection with Deep Learning: A Review. *ArXiv* **2019**, ArXiv180705511. Available online: http://arxiv.org/abs/1807.05511 (October 2020).